applied optics

Development and calibration of a high dynamic range and autonomous ocean-light instrument to measure sub-surface profiles in ice-covered waters

Bernhard Schartmüller,[1,*] Philip Anderson,[2] David McKee,[1,3] Stacey Connan-McGinty,[3] Tomasz P. Kopec,[1] Malin Daase,[1,4] Geir Johnsen,[4,5] and Jørgen Berge[1]

[1]Department of Arctic and Marine Biology, Faculty of Biosciences, Fisheries and Econonomics, UiT The Arctic University of Norway, NO-9037, Tromsø, Norway
[2]Scottish Association for Marine Science (SAMS), Scottish Marine Institute, Oban, UK
[3]Physics Department,University of Strathclyde , Glasgow, Scotland, UK
[4]The University Centre in Svalbard (UNIS), P.O. Box 156, NO-9171 Longyearbyen, Norway
[5]Centre for Autonomous Marine Operations and Systems, Department of Biology, Norwegian University of Science and Technology (NTNU), Trondheim Biological Station, NO-7491 Trondheim, Norway
*bernhard.schartmueller@uit.no

Received 3 August 2023; revised 20 September 2023; accepted 20 September 2023; posted 20 September 2023; published 23 October 2023

The optical chain and logger (OptiCAL) is an autonomous ice-tethered observatory equipped with multiple light sensors for mapping the variation of light with depth. We describe the instrument and present an ensemble calibration for downwelling irradiance E_{PAR} in [μmol $m^{-2}s^{-1}$]. Results from a long-term deployment in the Arctic Ocean demonstrate that the OptiCAL can cover the high dynamic range of under-ice light levels from July to November and produce realistic values in terms of magnitude when compared to modeled surface irradiance. Transient features of raised light levels at specific depths associated with nearby leads in the ice underline the importance of depth-resolved light measurements.

https://doi.org/10.1364/AO.502437

1. INTRODUCTION

Sea ice in the Arctic and the Antarctic form one of the largest ecosystems on Earth [1]. It provides microhabitats for algal communities and supports a wide range of organisms [1–3]. However, the ice structure is temperature-dependent and shows substantial spatial and temporal variability [4]. Light transmission through sea ice and snow is highly variable [4–6] and determines how much of the incoming surface light reaches the water column below the sea ice. Light is a limiting factor when it comes to the timing of phytoplankton and sea ice algae blooms in the Arctic [7,8] and in the Antarctic [9]. At the same time, too much light can be also a stress factor for primary producers [7]. This means that the light climate, consisting of irradiance, spectral irradiance, and the length of exposure (photoperiod), is crucial for marine biological processes and ecosystems [10]. Therefore, it is important to measure light continuously and with depth resolution throughout seasonal cycles.

Light also regulates predator–prey interactions [11] and governs processes such as the diel vertical migration (DVM) of zooplankton, probably the largest synchronized movement of biomass on the planet [12]. Studies have shown that DVM occurs even during the polar night, in response to variations in solar and lunar illumination that are far below the threshold of human perception [13–15]. However, measuring these light levels is challenging, as only a limited number of commercially available light sensors are currently able to do so.

Recording the light climate dynamics is necessary for understanding how Arctic and Antarctic ecosystems work, but it is also a difficult task. The remoteness of the location and the harsh physical conditions set limitations on equipment and researchers in these areas and numerical models [16] and satellite products are therefore widely used for estimating the light climate [17]. The moderate resolution imaging spectroradiometer (MODIS) and the ocean and land color instrument (OLCI) are two examples of satellite sensors that can provide photosynthetically active radiation (PAR) [18,19]. Reanalysis products

such as ERA5 can provide shortwave radiation [20]. Although these products are able to quantify large-scale changes, complementary *in situ* measurements are still necessary [21]. The ArcLight observatory on Svalbard in the Arctic provides such *in situ* light climate measurements continuously for air [10]. However, as large areas in the Arctic and the Antarctic are ocean, different platforms are needed for the marine environment.

Ice-tethered observatories (ITOs) are an established platform for measuring interannual variations *in situ* and are flexible with respect to which sensors they can carry. The Warming and iRadiance Measurements buoys engineered by Pacific Gyre Inc. [21,22] and Woods Hole Oceanographic Institution bio-optical ice-tethered profilers [23,24] are two examples of ITOs that can carry light sensors. However, both designs use "standard" light sensors that have limited sensitivity, restricting how far measurements can be made in terms of either depth or season. The optical chain and logger (OptiCAL) is presented here as an important addition to the existing ITOs for mapping the light climate in the polar regions over an extended range of irradiance levels.

2. METHODS

The OptiCAL is an autonomous ice-tethered observatory designed for mapping the under-ice light climate across a greater dynamic range than has previously been possible. The chain comprises of up to 32 "nodes" deployed along a power/communication cable [Fig. 1(a)]. Each node has six optical sensors, three facing vertically up (to detect downwelling light) and three facing down (for upwelling light). Two of the three sensors in each set have gel filters, orange or blue, with the third sensor being unfiltered [Fig. 1(b)]. This paper focuses exclusively on the unfiltered sensor for measuring downwelling E_{PAR} [irradiance in the photosynthetic active radiation (PAR) wavelength range].

As seen in Fig. 1(b), the long axis of the ellipsoidal node is aligned with the cable, and therefore sits in the water "pointing" up and down. The sensors have opaque baffles (non-transparent sheeting) directly behind them, and the circuit board (PCB) is also opaque. These baffles and PCBs are painted white for the upper sensors (which look upward and measure downwelling E_{PAR}) and black for the lower units (which detect upwelling E_{PAR}). This design has a double function: the upper sensors "see" either the ocean surface, or the white paint, which is illuminated by the surface, roughly doubling the sensitivity. The lower sensors, however, must only detect the much dimmer upwelling E_{PAR} (ca. 1/100 of the downwelling E_{PAR}), so the baffles and local PCB areas are painted black to prevent inadvertent scattering of downwelling E_{PAR} into these down-looking sensors.

The chain of nodes hangs vertically under a spar buoy which has a "slim" design to avoid shading of the upward-looking sensors. The OptiCAL is designed to float vertically when the chain and buoy are free from the ice. The buoy houses a set of alkaline batteries, a logger/controller unit, and telemetry. Data are transmitted by satellite communication to a land-based data server and archive.

The nodes on the chain are energized for ca. 15 s, during which time each node samples the light levels and stores the data temporarily. The logging interval is therefore controlled by the logger/controller, and overall power drain is mainly dependent on this interval. When the node capture period is complete, the controller sequentially polls the nodes on the chain, sending addressed commands to each node to request the data to be relayed back to the buoy. This takes < 1 s. Once data are retrieved from all nodes, the power to the chain is terminated.

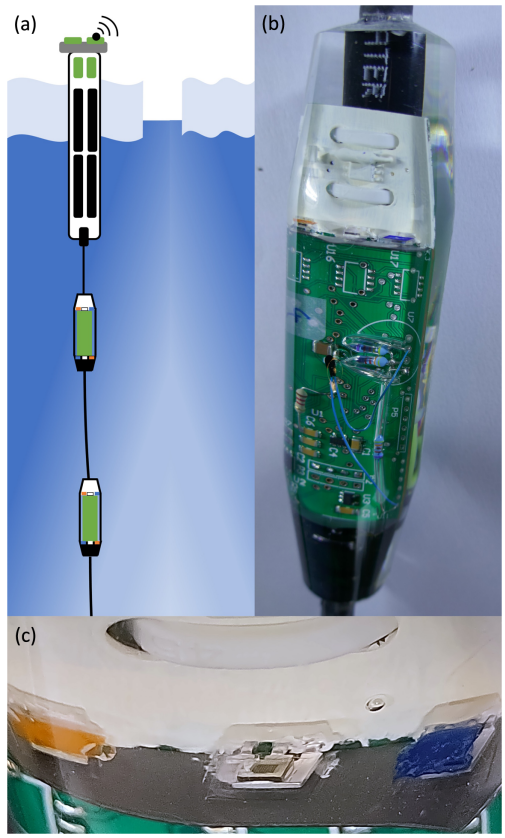

Fig. 1. (a) Illustration of the OptiCAL system consisting of a spar buoy (containing iridium and GPS antenna, logger/controller, iridium modem and batteries) fixed in sea ice and a chain with several OptiCAL nodes in the water column. (b) Picture of an OptiCAL node. Three sensors next to a white reflector facing upward are measuring downwelling light and three sensors next to a blackreflector facing downward are measuring upwelling light. The electronics including the sensors are ingrained in a transparent resin. (c) Close-up of upward-facing sensors. The unfiltered sensor for measuring E_{PAR} in the middle and the two sensors with blue and orange gel filters on the side.

Node data are combined with other house-keeping information, including position and time from GPS, and held in a buffer ready for onward transmission. Transmission is attempted when both the buffer has one or more full "data packets" and the satellite reception signal is strong. Data packet size is dependent upon the chosen satellite system in order to minimize costs (all "packets" contain viable data). The buffer system is therefore a soft-boundary first-in-first-out, where the start and end of the chain sample does not necessarily match the start or end of the satellite data packet. Records are recovered at the land-based data server, and data integrity is checked prior to analysis.

The OptiCAL nodes use light-to-frequency converters that consist of a silicon photodiode and a current-to-frequency

converter on a single monolithic complementary metal–oxide–semiconductor integrated circuit [25]. The output is a square wave, and its frequency is close to directly proportional to light intensity (irradiance) on the photodiode [25]. Note that in earlier versions of the OptiCAL the raw data represents the number of edges, that is both the rising and the falling of the square waves. This means that if the sensor is transmitting a 10 Hz square wave, the node would record "20 edge counts" for the earlier versions. The sensor responds over the wavelength range from 320 to 1050 nm and is temperature compensated from 320 to 700 nm [25]. The operating temperature from −25°C to 70°C [25] makes it suitable for all marine environments, including polar regions.

In Fig. 2 the spectral responsivity of the OptiCAL node sensor is compared to an "ideal" E_{PAR} sensor response, which is a constant normalized spectral responsivity equal to one in the wavelength range from 400 to 700 nm. This means that an ideal E_{PAR} sensor has the same responsivity in the PAR range independent of the wavelength (red line in Fig. 2). The Satlantic PAR-LOG irradiance-cosine-in-water (ICSW) that was used for calibration has a wavelength response close to the ideal E_{PAR} response [26], although small deviations remain. Typically, this responsivity is obtained by careful selection of filters for E_{PAR} sensors.

In contrast, the OptiCAL node sensor has no filter and has a much broader responsivity from 320 to 1050 nm (Fig. 2). However, for the comparison of spectral responsivity it is necessary to take the medium of operation (air, water) into consideration. While the difference between the two sensors is evident for air, the difference in water is expected to be much smaller. Red and infrared light are absorbed quickly in water. The same, although to a smaller extent, is true for UV light. Hence, we assume that the spectral responsivity of the two sensors in sea water is similar enough to justify attempting a cross calibration for the OptiCAL nodes.

3. RESULTS

The aim of this paper is to generate a robust calibration for the unfiltered sensors of the OptiCAL nodes that converts the raw sensor count from the unit millihertz [mHz] to E_{PAR} in [μmol m^{-2}s^{-1}]. We begin by assessing sensor consistency to establish if an ensemble calibration is feasible rather than calibrating each node separately.

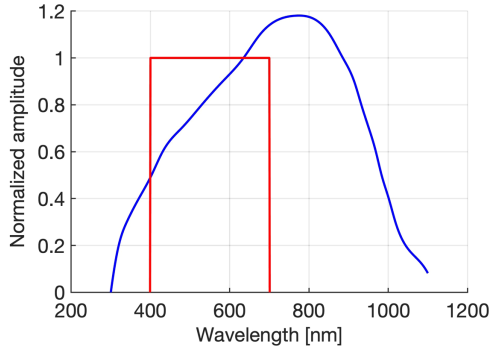

Fig. 2. Spectral responsivity (blue line) of the sensor used in the OptiCAL nodes (line traced after Fig. 10 in product document [25] using MATLAB). The red line represents an ideal PAR wavelength response.

A. Inter-Sensor Similarity

There are two possible ways of calibrating the OptiCAL nodes dependent on the similarity in light response of the sensors. If the inter-sensor similarity is high, a "global" or "ensemble" calibration can be applied. This means that one calibration is good enough for all sensors. Otherwise, a calibration must be derived for each sensor individually, which might increase the accuracy but requires a lot more time. To determine if a global calibration is feasible, inter-sensor similarity was tested by deploying 11 OptiCAL nodes in a calibration cage on a roof with minimal shadowing [Fig. 3(a)]. Data was recorded over 3 and a half days. Obvious outliers, non-contiguous data, and data close to sensitivity threshold and saturation were removed. The resulting 2970 data points for each sensor are shown in the time series in Fig. 3(b).

The inter-sensor variability was estimated by plotting the signals from individual nodes against the mean of all the nodes in Fig. 3(c). Note that there appears to be a gap in the data around 10^7 [mHz]. Analysis of the operating system revealed an error when switching gain settings. This has been rectified in later versions of the OptiCAL and is found to have minimal

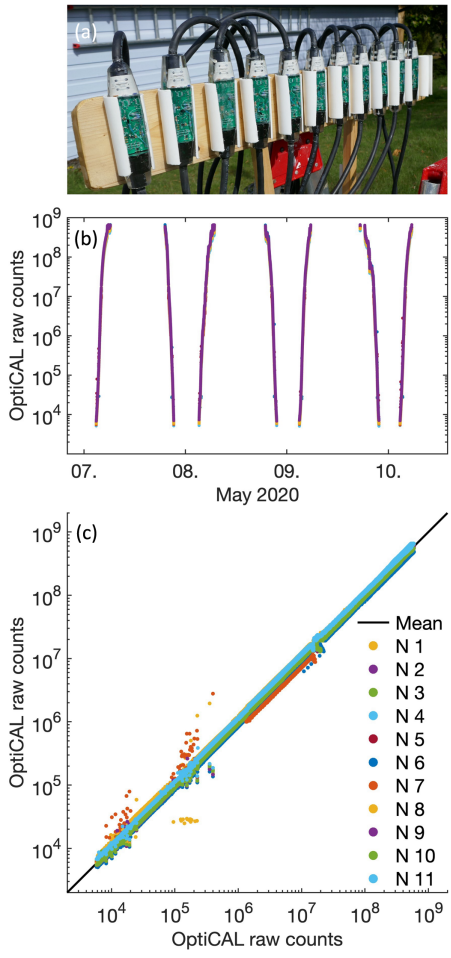

Fig. 3. (a) Setup of 11 OptiCAL nodes mounted on a frame for testing the internode variability. (b) Multiple day time series for 11 sensors. Outliers, saturated data, and data below the sensitivity threshold were removed. (c) Individual OptiCAL nodes (legend indicates node numbers) plotted against the mean of all nodes (1:1 line).

impact on the data presented here from the original version of the instrument.

The high dynamic range of the OptiCAL required logarithmic scaled axes. The relative error is ± 17.1%, but very few data points come close to these limits. Therefore, quantiles are a more descriptive parameter. 99% of observations for the relative error lie in the interval [−2.5%, 1.9%]. Given the focus of effort is to try to cover the broadest dynamic range possible, covering many orders of magnitude this level of inter-sensor variability is deemed to be acceptable for an ensemble approach.

B. Dark Current

The signal measured by optical sensors, S_M, usually consists of two parts: a background dark signal, S_D, and the signal caused by presence of light, S_L:

$$S_M = S_D + S_L. \quad (1)$$

The aim of calibration is to convert the light signal into calibrated units providing absolute irradiance in [µmol $m^{-2}s^{-1}$]. Typically, the dark signal is measured in a dark calibration chamber and subtracted from the measured signal. According to the product document [25], the sensor used in the OptiCAL nodes has a low dark frequency of typically 400 [mHz]. However, analysis of data from deep ocean profiles during the polar night demonstrate that during the darkest periods of the polar night the sensors did not trigger. Therefore, we assume for sensor calibration that the dark current is sufficiently close to zero that we can set it to zero for calibration purposes.

C. Generation of in situ Match-Ups between OptiCAL and Profiling Satlantic E_{PAR} Measurements

The calibration factor was derived from comparisons with *in situ* profiles of E_{PAR} from ship deployments on a cruise on the research vessel R/V Helmer Hanssen in 2020. Co-temporal and near co-spatial optical data were collected from both a 50 m OptiCAL chain with handheld logger and a conductivity temperature and depth (CTD) profiler equipped with a Satlantic PAR-LOG ICSW sensor. Both the OptiCAL and the CTD profiler were deployed from a Polarcirkel workboat. The purpose was to gather sufficient measurements to derive a calibration factor for converting the OptiCAL raw data from [mHz] to E_{PAR} [µmol $m^{-2}s^{-1}$] and make an estimate of the uncertainty of the measurements.

The deployments were at three locations in the Svalbard archipelago, Kongsfjorden, Smeerenburgfjorden and Rijpfjorden, between 8 and 12 September 2020. For these deployments the OptiCAL chain provided a time series of observations at discrete depths (targeted depths were 1, 2, 3, 4, 5, 6, 7, 14, 21, 32, and 50 m), while the profiling E_{PAR} sensor produced a series of depth profiles (for most datasets 10). Figure 4 shows an example of co-temporal OptiCAL and CTD E_{PAR} data for one of the stations, taken on the morning of 11 September 2020.

With both the CTD E_{PAR} depth profiles and the OptiCAL nodes being sampled at discrete but differing time intervals and similarly at discrete but differing depths, interpolation between the gridded datasets was required. The following method acknowledges that the CTD E_{PAR} profile data have a higher time

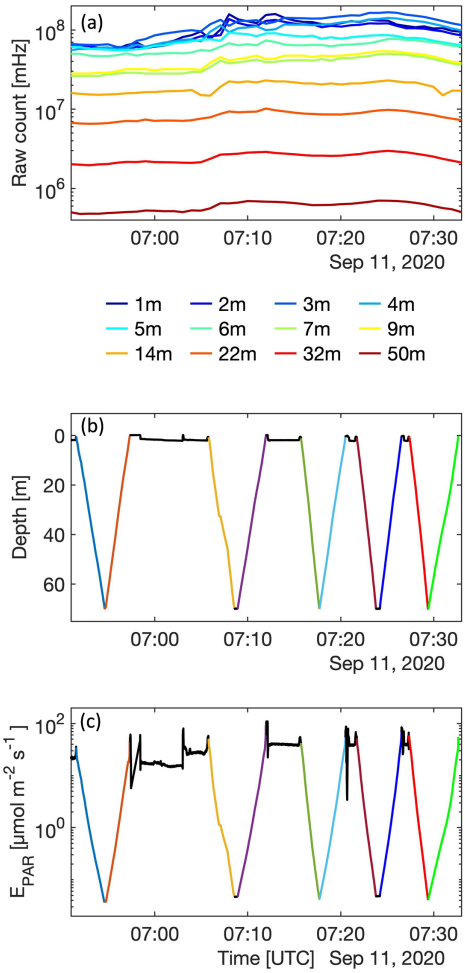

Fig. 4. (a) Time series of the OptiCAL raw data collected at Smeerenburgfjorden on 11th September 2020. Initial noise during deployment was removed. Raw counts show slight increase with time. (b) Time series for depth of the 10 CTD E_{PAR} casts (upcasts and downcasts) co-temporal with the OptiCAL data. Colored data indicate casts used for generation of match-ups between OptiCAL and profiling Satlantic E_{PAR} measurements. (c). Time series for E_{PAR} of the 10 CTD E_{PAR} casts (upcasts and downcasts) co-temporal with the OptiCAL data. Colored data indicate casts used for generation of match-ups between OptiCAL and profiling Satlantic E_{PAR} measurements.

and depth resolution than the OptiCAL data due to the high sampling rate/slow profile rate. There are therefore many more CTD E_{PAR} data per cast than OptiCAL data. Simple re-gridding of the OptiCAL data onto the CTD E_{PAR} data is not ideal, as this biases deeper OptiCAL nodes with more CTD E_{PAR} data per node. Simple regression also generates bias in any subsequent regression in the log domain because the linear re-gridding generates spurious inter-level curvature in the profiles in log-log space.

The solution used is to select the CTD E_{PAR} measurement that is depth-wise closest to the selected OptiCAL node depth. The corresponding OptiCAL count estimation for the CTD E_{PAR} datum is taken from linear interpolation of the four most adjacent OptiCAL datums. This procedure is repeated for each OptiCAL node depth and all casts. The selection is based on "nearest depth" rather than "nearest time" as this minimizes

residual error from curvature. Observation of the OptiCAL count surfaces shows that the change in OptiCAL count per depth step is greater than change per time step.

The interpolation resulted in (for most cast sets) 10 data points at each of the 12 OptiCAL levels. The *in situ* matchups between OptiCAL and profiling CTD E_{PAR} measurements form the basis for selecting an appropriate regression model and deriving a calibration factor.

D. Regression Method

The sensors used in the OptiCAL show a linear relation between irradiance and frequency for the wavelength 635 nm [25]. This, together with a relatively equally balanced spectral responsivity in the PAR wavelength range (Fig. 2), implies an underlying linear relation between the recorded OptiCAL counts and E_{PAR} and favors simple linear regression for the selection of an appropriate model.

However, as regressions are driven by mean values and our data spans three decades on a log scale, simple linear regression would be biased toward the upper (near-surface) levels. The deep ocean data would be effectively weighted close to zero. To remove this orders of magnitude variability and to make the dataset better balanced for further regression, both data groups were log transformed with the common (base 10) log, resulting in Eq. (2). For deriving a calibration factor, the function must be retransformed back into linear space [Eqs. (2)–(6)]:

$$\log_{10}(y) = p_1 \cdot \log_{10}(x) + p_2, \tag{2}$$

$$\log_{10}(y) = p_1 \cdot \log_{10}(x) + \log_{10}(m), \tag{3}$$

$$\log_{10}(y) = \log_{10}\left(x^{p_1}\right) + \log_{10}(m), \tag{4}$$

$$\log_{10}(y) = \log_{10}\left(m \cdot x^{p_1}\right), \tag{5}$$

$$y = m \cdot x^{p_1}. \tag{6}$$

The result is a power law [Eq. (6)]. However, there is the risk that the data are linear, but noisy, and with few data points, the least-squares method may give a best fit with a slightly non-unity p_1 and a slightly incorrect p_2. However, based on the datasheet of the producer [25] we assume a genuine "linear" relation between x and y. Hence, p_1 must be unity. The calibration factor can then be directly calculated from $p_2 = \text{mean}(\log_{10}(y) - \log_{10}(x))$. We call this the "difference" regression method. Figure 5 shows the "difference" regression method applied to *in situ* match-ups between OptiCAL and CTD E_{PAR} data for the Smeerenburgfjorden dataset (Fig. 4).

E. Ensemble Calibration

A total of five successful cast sessions were collected during the R/V Helmer Hanssen 2020 cruise. Data were quality controlled and interpolated to form match-ups following the procedure outlined in Section 3.C. To produce a single ensemble calibration, all usable data were plotted, and the "difference" regression method was applied in Fig. 6. The resulting calibration factor with 95% prediction interval $(3.4518 \pm 0.078) \cdot 10^{-7}$ can be used for converting the OptiCAL data from [mHz] to [μmolm^{-2}s^{-1}]. For earlier versions of the OptiCAL such as those deployed during the MOSAiC expedition [27] a calibration factor of $(1.7259 \pm 0.039) \cdot 10^{-7}$ can be used for converting data from [edge counts] to [μmolm^{-2}s^{-1}].

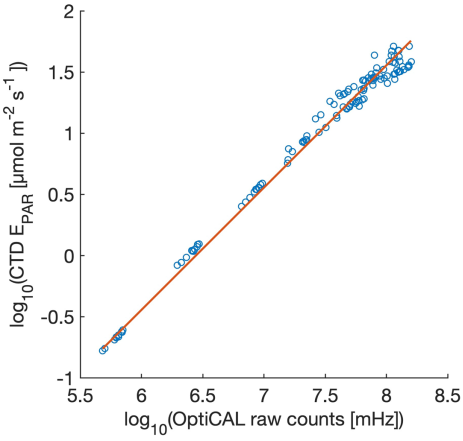

Fig. 5. "Difference" method regression of $\log_{10}$ CTD E_{PAR} against $\log_{10}$ OptiCAL raw counts. The depth grouping is apparent, but due to the pseudo-log node depths, the data groups are evenly distributed.

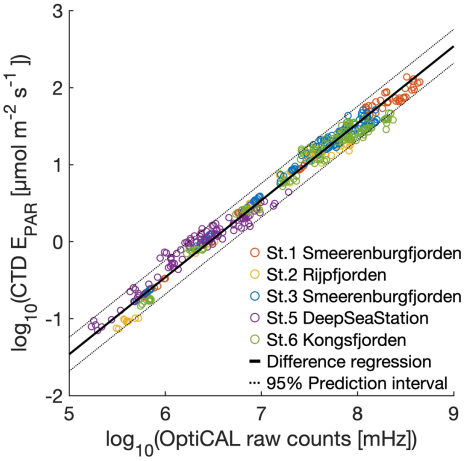

Fig. 6. Ensemble calibration. All usable data were plotted in one plot and a "difference" method linear regression was applied for deriving a calibration factor.

F. Field Demonstration

To test if the OptiCAL achieves the stated goal of providing the magnitude of quantitative E_{PAR} data in ice-covered waters, we applied the calibration factor to field data collected by an OptiCAL with seven nodes, which was deployed in the Arctic Ocean at 84.64°N 28.72°E by the Norwegian research vessel RV Kronprins Haakon in 2019 (AO2019 deployment). We received data from 13 July 2019 until 14 December 2019 when contact was lost. The last known position was 82.65°N 12.54°E. The OptiCAL was deployed together with other

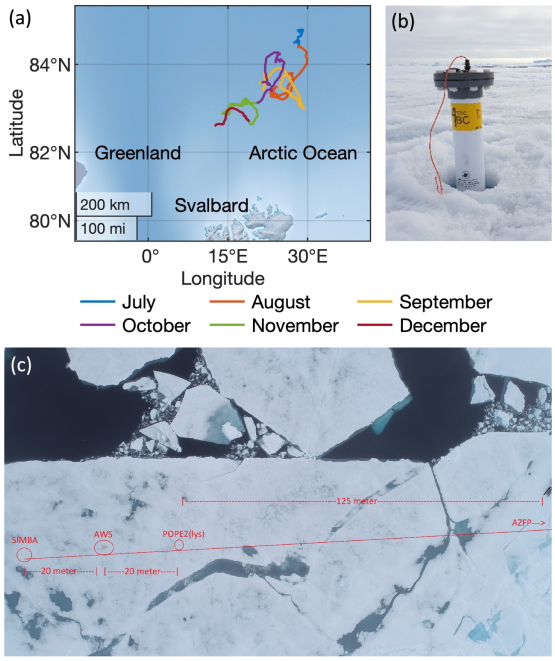

Fig. 7. (a) Map showing the drift track of the OptiCAL that was deployed in the Arctic Ocean on the AO2019 cruise (map created with MATLAB Mapping Toolbox). (b) Surface part of OptiCAL and ice conditions at time of deployment. Picture credit: Kunuk Lennert/UiT. (c) Aerial image of deployment site on 13 July 2019 23:45. Note open water, refrozen leads/melt ponds in proximity of the OptiCAL. Instruments are marked with red circles. The OPTICAL is called POPE2(lys) in the picture. Picture credit: Kunuk Lennert/UiT.

ITOs on an ice floe, including a snow ice mass balance apparatus (SIMBA) unit [28], an automatic weather station, and an acoustic zooplankton fish profiler. Since GPS data was partly missing for the OptiCAL, we used GPS coordinates from a XEOS GPS beacon mounted on an ITO that was drifting close to the OptiCAL until the OptiCAL stopped working. See Fig. 7 for the drift track of the OptiCAL and for pictures of the ice conditions at the time of deployment.

The time series in Fig. 8(a) shows the measured downwelling irradiance E_{PAR} for each OptiCAL node, the surface irradiance predicted by the HEIMDALL radiative transfer model [16] using ERA5 cloud data [29], the solar and lunar zenith angle, and the SIMBA-derived snow and ice thickness. The general trend is that light levels decrease with increasing water depth. However, for periods we observe higher light levels at 6 m depth compared to shallower depths. Since the time series shows that these features are transient, we interpret these features as being associated with a nearby lead or possibly a melt pond. In this context, "nearby" means roughly the same distance as the depth of the OptiCAL node that measures the highest light intensity, the idea being that the upper OptiCAL nodes are under a local umbrella of sea ice floe (which causes a shadow), while light penetrating a nearby lead or other gap is shining directly on the nodes lower down. Even deeper, the light is attenuated as normal. Based on an aerial image of the deployment site in Fig. 7(c) we measured the distance to the closest lead/melt ponds. The distance was 8.65 m, while most sub-surface maxima in the E_{PAR} profiles occurred at 6 m, which is a similar distance. Sub-surface

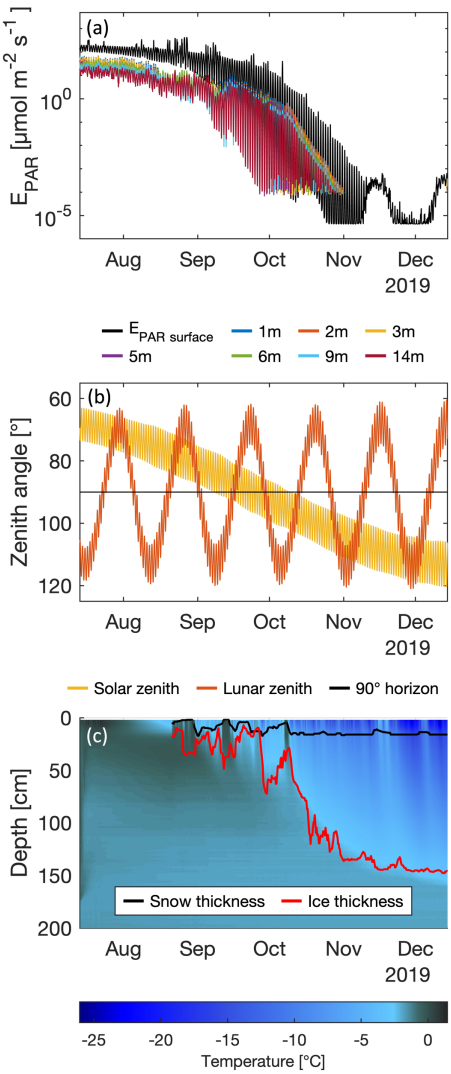

Fig. 8. (a) E_{PAR} time series for OptiCAL and above surface irradiance E_{PAR} from HEIMDALL model using ERA5 cloud data. (b) Solar and lunar zenith angles and 90° horizon. (c) Temperature profile time series from SIMBA unit and derived snow and ice thickness lines. Note that the unit produced occasionally for periods of time unrealistic values for temperature. These were then replaced by interpolated values that were calculated based on the surrounding temperature profiles.

irradiance maxima are an interesting feature as they might influence primary production [30]. Their occurrence stresses the importance for depth-resolved light measurements.

The time series shows that the OptiCAL nodes have a sufficient dynamic range to measure the under-ice light levels from the date of deployment on 13 July 2019 until 28 October 2019 down to 14 m depth and until 02 November 2019 at 1 m depth. Later, light levels were below the sensitivity threshold of the OptiCAL nodes. All OptiCAL nodes in this deployment were able to measure down to at least $9.2e^{-05}$ µmol m^{-2}s^{-1}. However, on 14 December 2019 the light levels rose for several hours above the sensitivity threshold for the OptiCAL nodes down to 9 m depth. Shortly after, the connection to the OptiCAL was lost. Based on this data we suspect that the ice broke up on 14 December 2019 and consequently more light was entering the water column. After this, the light levels sank

again below the sensitivity threshold of the OptiCAL nodes. This could be due to the ice coming together again and shadowing the OptiCAL nodes. Shortly afterwards contact with the OptiCAL was lost. The ice could have crushed or damaged the OptiCAL and therefore contact was lost. This hypothesis is supported by the GPS positions of other ITOs that were deployed together with the OptiCAL. All of them drifted together until 14 December 2019. On this day the ITOs separated. It is likely that ice breakup caused this separation.

A comparison of the calibrated OptiCAL measurements to HEIMDALL modeled surface irradiance using ERA5 cloud data [29] in Fig. 8, shows that the trends of both time series have a large degree of congruence. The solar zenith angle is the dominating factor, determining the irradiance levels until mid-October, but as the Sun sinks below the horizon the lunar zenith angle takes over. To check if the observed light levels seem realistic in comparison with the HEIMDALL model, we calculated the mean transmittance, more precisely the proportion of the mean irradiance measured by the OptiCAL at 1 m depth to the mean modeled surface irradiance for the period from 13 July 2019 to 28 September 2019. For that we simulated three different surface irradiance datasets. One for constant clear sky, one for constant cloud covered skies, and one with varying local cloud conditions predicted by ERA5 cloud data [29]. Depending on the cloud coverage the mean transmittance ranges from 0.06 for constant clear sky to 0.20 for a constantly cloud covered sky. For the ERA5 cloud product it amounts to 0.17. Perovich [4] gives an example for the spatial change in transmittance along a short transect covering both ponded ice and bare ice. The pond transmittance (0.45) was almost an order of magnitude larger than bare ice transmittance (0.05) [4]. Although a comparison of transmittance is not possible because of the large spatial and temporal variations, the order of magnitude of the mean transmittance for our deployment seems realistic compared to this example. Our mean transmittance values also lie within (for the simulation of constantly cloud covered sky slightly above) the range of transmittance values from 0.004 to 0.198, averaged over larger areas from ROV missions [31]. However, mean transmittance varies a lot with surface conditions, snow depth, and ice thickness and consequently is an intrinsically limited descriptor of ice optical properties [4].

The SIMBA unit provided us with snow and ice thickness data approximately 40 m away from the OptiCAL measuring site. The ice thickness at the date of deployment was calculated (using equations from [32]) to be 32 cm and increased (with intermediate melting and freezing periods) to 128 cm on 02 November 2019. Snow thickness varied between 2 and 17 cm. This means that the OptiCAL is sensitive enough for measuring the low E_{PAR} values in thick ice when the Sun is 7.9° below the horizon.

4. SUMMARY AND DISCUSSION

The design of the OptiCAL, using sensors consisting of a photodiode ingrained in a resin, but with no light diffusor or filter, is unorthodox for an E_{PAR} sensor. However, avoiding optical components that reduce the number of photons reaching the photodiode offers higher light sensitivity. This improves our capability to measure the low light levels prevailing in the ocean under sea ice during the polar night.

We analyzed the OptiCAL nodes for their similarity and deem an ensemble approach, treating them effectively as clones, for calibration purposes as sufficient. The initial calibration was derived from *in situ* comparison profiles of E_{PAR} from ship deployments near Svalbard in September 2020. The resulting calibration factor of $(3.4518 \pm 0.078) \cdot 10^7$ can be used to convert OptiCAL raw data from [mHz] to [μmol $m^{-2}s^{-1}$]. For earlier versions of the OptiCAL that provide raw data in [edge counts] use a calibration factor of $(1.7259 \pm 0.039) \cdot 10^{-7}$ for converting data to [$\mu molm^{-2}s^{-1}$].

Data from the Arctic Ocean (AO2019 deployment) confirmed that the OptiCAL nodes have a very high dynamic range, sufficient to cover the under-ice light levels during from July (midnight Sun) until the beginning of November (polar night). A comparison with the previously validated HEIMDALL model [16] indicates that the calibrated OptiCAL measurements are realistic in terms of magnitude, and that observed temporal signals are consistent with changing contributions of solar and lunar light contributions.

The field deployment proved that the OptiCAL is robust enough for long-term deployment in ice-covered waters. Nevertheless, contact with the OptiCAL was lost after approximately 5 months, possibly because of a sea ice breakup. There was also an issue with the GPS resulting in periods of missing data. Future versions are expected to address these issues and fix the error with switching gain settings that was described in Section 3.A.

The calibrated OptiCAL light data together with complementary measurements from other platforms have the potential to provide new insights into ecosystem functioning in the polar regions.

Funding. Senter for Autonome Marine Operasjoner og Systemer (223254); Norges Forskningsråd (245923, 276730, 300333).

Acknowledgment. We would like to thank Daniel Vogedes (UiT) and Kunuk Lennert (UiT) for the deployment of the instruments and the crews of the R/V Helmer Hanssen and R/V Kronprins Haakon for their assistance. Thanks also to Daniel Vogedes (UiT) for data collection and valuable comments on the paper and to Florian Schartmüller for valuable comments on the statistics.

Disclosures. The authors declare no conflicts of interest. The authors would still like to inform that Bernhard Schartmüller is on a leave from his position as an engineer at AkerSolutions AS. This paper is not supported financially or in any other way related to this company.

Data availability. All data used in this paper will be fully Open Access through National Infrastructure for Research Data (NIRD). Data for comparing the inter-node similarity are available in [33]. Data underlying the calibration results are available in [34]. The OptiCAL data and HEIMDALL modeled data for the field demonstration are available in [35]. The temperature, snow- and ice-thickness data for the field demonstration (AO2019 deployment) will be published as part of a paper (currently in preparation) led by Daase. Until these data are published, the data are available from the first author on request.

REFERENCES

1. K. R. Arrigo, "Sea ice as a habitat for primary producers," in *Sea Ice* (Wiley Online Library, 2017), pp. 352–369.
2. D. A. Caron, R. J. Gast, and M. È. Garneau, "Sea ice as a habitat for micrograzers," in *Sea Ice* (Wiley Online Library, 2017), pp. 370–393.

3. B. A. Bluhm, K. M. Swadling, and R. Gradinger, "Sea ice as a habitat for macrograzers," in *Sea Ice* (Wiley Online Library, 2017), pp. 394–414.
4. D. K. Perovich, "Sea ice and sunlight," in *Sea Ice* (Wiley Online Library, 2017), pp. 110–137.
5. M. G. Cooper, L. C. Smith, A. K. Rennermalm, M. Tedesco, R. Muthyala, S. Z. Leidman, S. E. Moustafa, and J. V. Fayne, "Spectral attenuation coefficients from measurements of light transmission in bare ice on the Greenland Ice Sheet," Cryosphere **15**, 1931–1953 (2021).
6. T. C. Grenfell and G. A. Maykut, "The optical properties of ice and snow in the Arctic basin," J. Glaciol. **18**, 445–463 (1977).
7. H. Hop and C. Wiencke, "The Ecosystem of Kongsfjorden, Svalbard," in *The Ecosystem of Kongsfjorden, Svalbard* (Springer, 2019), pp. 1–20.
8. E. Leu, C. Mundy, P. Assmy, K. Campbell, T. Gabrielsen, M. Gosselin, T. Juul-Pedersen, and R. Gradinger, "Arctic spring awakening–Steering principles behind the phenology of vernal ice algal blooms," Prog. Oceanogr. **139**, 151–170 (2015).
9. B. Raymond, K. Meiners, C. W. Fowler, B. Pasquer, G. D. Williams, and S. Nicol, "Cumulative solar irradiance and potential large-scale sea ice algae distribution off East Antarctica (30°E–150°E)," Polar Biol. **32**, 443–452 (2009).
10. G. Johnsen, A. Zolich, S. Grant, R. Bjørgum, J. H. Cohen, D. McKee, T. P. Kopec, D. Vogedes, and J. Berge, "All-sky camera system providing high temporal resolution annual timeseries of irradiance in the Arctic," Appl. Opt. **60**, 6456–6468 (2021).
11. L. Hobbs, N. S. Banas, J. H. Cohen, F. R. Cottier, J. Berge, and Ø. Varpe, "A marine zooplankton community vertically structured by light across diel to interannual timescales," Biol. Lett. **17**, 20200810 (2021).
12. G. C. Hays, "A review of the adaptive significance and ecosystem consequences of zooplankton diel vertical migrations," in *Migrations and Dispersal of Marine Organisms*, M. B. Jones, A. Ingólfsson, E. Ólafsson, G. V. Helgason, K. Gunnarsson, and J. Svavarsson, eds., Vol. **174** of Developments in Hydrobiology (Springer2003), pp. 163–170.
13. J. Berge, F. Cottier, K. S. Last, Ø. Varpe, E. Leu, J. Søreide, K. Eiane, S. Falk-Petersen, K. Willis, and H. Nygård, "Diel vertical migration of Arctic zooplankton during the polar night," Biol. Lett. **5**, 69–72 (2009).
14. L. Hobbs, F. Cottier, K. Last, and J. Berge, "Pan-Arctic diel vertical migration during the polar night," Mar. Ecol. Prog. Ser. **605**, 61–72 (2018).
15. J. H. Cohen, K. S. Last, C. L. Charpentier, F. Cottier, M. Daase, L. Hobbs, G. Johnsen, and J. Berge, "Photophysiological cycles in Arctic krill are entrained by weak midday twilight during the Polar Night," PLoS Biol. **19**, e3001413 (2021).
16. S. Connan-McGinty, N. S. Banas, J. Berge, F. Cottier, S. Grant, G. Johnsen, T. P. Kopec, M. Porter, and D. McKee, "Midnight sun to polar night: a model of seasonal light in the Barents Sea," J. Adv. Model. Earth Syst. **14**, e2022MS003198 (2022).
17. G. Castellani, G. Veyssière, M. Karcher, J. Stroeve, S. N. Banas, A. H. Bouman, S. A. Brierley, S. Connan, F. Cottier, F. Große, L. Hobbs, C. Katlein, B. Light, D. McKee, A. Orkney, R. Proud, and V. Schourup-Kristensen, "Shine a light: under-ice light and its ecological implications in a changing Arctic Ocean," Ambio **51**, 307–317 (2022).
18. National Aeronautics and Space Administration (NASA), "MODIS daily mean photosynthetically available radiation," 2023, https://modis.gsfc.nasa.gov/data/dataprod/par.php.
19. ARGANS, "OLCI Level 2 Algorithm Theoretical Basis Document Photosynthetically Active Radiation," Tech. Rep. (2010).
20. European Centre for Medium-Range Weather Forecasts, "Surface short-wave (solar) radiation downwards," 2010, https://codes.ecmwf.int/grib/param-db/?id=169.
21. C. M. Lee, M. DeGrandpre, J. Guthrie, V. Hill, R. Kwok, J. Morison, C. J. Cox, H. Singh, T. P. Stanton, and J. Wilkinson, "Emerging technologies and approaches for in situ, autonomous observing in the arctic," Oceanography **35**, 210–221 (2022).
22. V. J. Hill, B. Light, M. Steele, and R. C. Zimmerman, "Light availability and phytoplankton growth beneath Arctic sea ice: Integrating observations and modeling," J. Geophys. Res. Oceans **123**, 3651–3667 (2018).
23. S. R. Laney, R. A. Krishfield, and J. M. Toole, "The euphotic zone under Arctic Ocean sea ice: vertical extents and seasonal trends," Limnol. Oceanogr. **62**, 1910–1934 (2017).
24. S. R. Laney, R. A. Krishfield, J. M. Toole, T. R. Hammar, C. J. Ashjian, and M.-L. Timmermans, "Assessing algal biomass and bio-optical distributions in perennially ice-covered polar ocean ecosystems," Polar Sci. **8**, 73–85 (2014).
25. ams-AG, "Product document TSL235R light-to-frequency converter," ams OSRAM Group, 2018, https://ams.com/documents/20143/36005/TSL235R_DS000120_3-00.pdf/d267ee56-5494-c92d-8705-716becdd4051.
26. Sea-Bird-Scientific, "PAR photosynthetically active radiation sensor," 2022, https://www.seabird.com/asset-get.download.jsa?id=54627862136.
27. C. J. M. Hoppe, N. Fuchs, D. Notz, *et al.*, "A new lower limit for photosynthetic light requirements detected in Arctic microalgae," (to be submitted) (2023).
28. SAMS-Enterprise, "Autonomous snow and ice measurement," 2023, https://www.sams-enterprise.com/services/autonomous-ice-measurement/.
29. H. Hersbach, B. Bell, P. Berrisford, G. Biavati, A. Horányi, J. Muñoz Sabater, J. Nicolas, C. Peubey, R. Radu, I. Rozum, D. Schepers, A. Simmons, C. Soci, D. Dee, and J.-N. Thépaut, "ERA5 hourly data on single levels from 1979 to present," Copernicus climate change service (C3S) climate data store (CDS) (2018), https://doi.org/10.24381/cds.adbb2d47.
30. M. Ardyna, C. Mundy, M. M. Mills, L. Oziel, P.-L. Grondin, L. Lacour, G. Verin, G. Van Dijken, J. Ras, and E. Alou-Font, "Environmental drivers of under-ice phytoplankton bloom dynamics in the Arctic Ocean," Elem. Sci. Anthropocene **8**, 30 (2020).
31. C. Katlein, S. Arndt, H. J. Belter, G. Castellani, and M. Nicolaus, "Seasonal evolution of light transmission distributions through arctic sea ice," J. Geophys. Res. Oceans **124**, 5418–5435 (2019).
32. Z. Liao, B. Cheng, J. Zhao, T. Vihma, K. Jackson, Q. Yang, Y. Yang, L. Zhang, Z. Li, and Y. Qiu, "Snow depth and ice thickness derived from SIMBA ice mass balance buoy data using an automated algorithm," Int. J. Dig. Earth **12**, 962–979 (2019).
33. P. Anderson, B. Schartmüller, D. L. Vogedes, T. P. Kopec, D. McKee, G. Johnsen, and J. Berge, "In-air time series for intercomparison of a 11 high dynamic range and autonomous ocean-light instruments (OptiCAL)," NIRD research data archive, 2023, https://doi.org/10.11582/2023.00111.
34. P. Anderson, B. Schartmüller, D. L. Vogedes, T. P. Kopec, E. J. Venables, D. McKee, G. Johnsen, and J. Berge, "Calibration data for a high dynamic range and autonomous ocean-light instrument (OptiCAL)," NIRD research data archive, 2023, https://doi.org/10.11582/2023.00112.
35. P. Anderson, B. Schartmüller, D. L. Vogedes, T. P. Kopec, K. Lennert, M. Daase, S. Connan-McGinty, D. McKee, G. Johnsen, and J. Berge, "Deployment of a high dynamic range and autonomous ocean-light instrument (OptiCAL) in the Arctic Ocean from July to December 2019 and corresponding surface irradiance (EPAR), solar and lunar zenith angles modelled with the HEIMDALL radiative transfer model," NIRD research data archive, 2023, https://doi.org/10.11582/2023.00110.